


Formation of a two-dimensional single-component correlated electron system and band engineering in the nickelate superconductor NdNiO₂

Yusuke Nomura ^{1,*}, Motoaki Hirayama,¹ Terumasa Tadano,² Yoshihide Yoshimoto,³ Kazuma Nakamura,⁴ and Ryotaro Arita^{1,5}

¹RIKEN Center for Emergent Matter Science, 2-1 Hirosawa, Wako, Saitama 351-0198, Japan

²Research Center for Magnetic and Spintronic Materials, National Institute for Materials Science, Tsukuba 305-0047, Japan

³Department of Computer Science, The University of Tokyo, 7-3-1 Hongo, Bunkyo-ku, Tokyo 113-0033, Japan

⁴Quantum Physics Section, Kyushu Institute of Technology, 1-1 Sensui-cho, Tobata, Kitakyushu, Fukuoka, 804-8550, Japan

⁵Department of Applied Physics, The University of Tokyo, 7-3-1 Hongo, Bunkyo-ku, Tokyo 113-8656, Japan



(Received 9 September 2019; published 26 November 2019)

Motivated by the recent experimental discovery of superconductivity in the infinite-layer nickelate Nd_{0.8}Sr_{0.2}NiO₂ [Li *et al.*, *Nature (London)* **572**, 624 (2019)], we study how the correlated Ni $3d_{x^2-y^2}$ electrons in the NiO₂ layer interact with the electrons in the Nd layer. We show that three orbitals are necessary to represent the electronic structure around the Fermi level: Ni $3d_{x^2-y^2}$, Nd $5d_{3z^2-r^2}$, and a bonding orbital made from an interstitial s orbital in the Nd layer and the Nd $5d_{xy}$ orbital. By constructing a three-orbital model for these states, we find that the hybridization between the Ni $3d_{x^2-y^2}$ state and the states in the Nd layer is tiny. We also find that the metallic screening by the Nd layer is not so effective in that it reduces the Hubbard U between the Ni $3d_{x^2-y^2}$ electrons just by 10%–20%. On the other hand, the electron-phonon coupling is not strong enough to mediate superconductivity of $T_c \sim 10$ K. These results indicate that NdNiO₂ hosts an almost isolated correlated $3d_{x^2-y^2}$ orbital system. We further study the possibility of realizing a more ideal single-orbital system in the Mott-Hubbard regime. We find that the Fermi pockets formed by the Nd-layer states dramatically shrink when the hybridization between the interstitial s state and Nd $5d_{xy}$ state becomes small. By an extensive materials search, we find that the Fermi pockets almost disappear in NaNd₂NiO₄ and NaCa₂NiO₃.

DOI: [10.1103/PhysRevB.100.205138](https://doi.org/10.1103/PhysRevB.100.205138)

I. INTRODUCTION

Since the discovery of high transition temperature (T_c) superconductivity in the cuprates [1], a wide variety of two-dimensional correlated materials including layered transition metal oxides, pnictides, chalcogenides, some heavy-fermion materials, and organic conductors have provided a unique playground for unconventional superconductivity [2]. Among them, the high- T_c cuprates are of great interest due to their remarkably simple electronic structure: the Fermi surface consists of only one two-dimensional band. Thus, one may expect that if just one correlated orbital makes a two-dimensional Fermi surface, high- T_c superconductivity will emerge [3–9].

However, it has been a great theoretical and experimental challenge to find an analog of the cuprates [10]. One possible candidate is vanadates, for which we can think of designing a d^1 analog of the cuprates [11–14]. However, it is not an easy task to separate the two-dimensional $3d_{xy}$ band from the $3d_{yz}$ and $3d_{zx}$ bands. While nickelates can be an interesting d^7 analog of the cuprates, we need to consider a special heterostructure to remove the $3d_{3z^2-r^2}$ band from the Fermi level [15–18]. More recently, Sr₂IrO₄ and Ba₂IrO₄ are attracting broad interest as a possible $5d$ analog of the cuprates [19–22]. While it has been recently reported that doped Sr₂IrO₄ exhibits spectroscopic signatures suggesting a

d -wave superconducting gap [23,24], a zero-resistance state has not yet been observed. It should be noted that the system cannot be regarded as an ideal single-orbital system in that not only the $j_{\text{eff}} = \frac{1}{2}$ state, but also $j_{\text{eff}} = \frac{3}{2}$ states are involved with the low-energy physics [25,26]. Therefore, “orbital distillation” [8] in two-dimensional correlated systems has been a key issue for realizing an analog of the cuprates.

Recently, Li *et al.* discovered that the infinite-layer nickelate NdNiO₂ exhibits superconductivity when Sr is doped [27]. It is interesting to note that NdNiO₂ is isostructural to the infinite-layer copper oxide CaCuO₂ which becomes a superconductor below $T_c = 110$ K by hole doping [28]. In this compound, Ni has square planar oxygen coordination and is expected to have a d^9 configuration. Due to the absence of the apical oxygen, the crystal field in NdNiO₂ is totally different from the octahedral ligand field. Notably, the energy level of the $3d_{3z^2-r^2}$ orbital becomes much lower than that of the $3d_{x^2-y^2}$ orbital, even lower than the orbitals labeled t_{2g} in the octahedral environment [29]. In this situation, only the $3d_{x^2-y^2}$ band among the five $3d$ bands intersects the Fermi level. While this is good news for designing an analog of the cuprates, the previous calculations based on density functional theory (DFT) pointed out that there are two complications [29–33]. One is that electrons in the Nd layer make additional Fermi pockets. The other is that the charge-transfer gap between the transition metal $3d$ states and O $2p$ states is larger than that in the cuprates.

*yusuke.nomura@riken.jp

In this paper, we focus on the first problem, i.e., the role of the “additional” Nd $5d$ Fermi pockets which are absent in the cuprates. Especially, we discuss the following issues of critical importance: (i) What is the minimal model to describe these additional degrees of freedom in the Nd layer? (ii) Does the hybridization between the Ni $3d_{x^2-y^2}$ band and these additional bands invalidate the effective single-band $3d_{x^2-y^2}$ model? (iii) Does the metallic screening from the additional Fermi pockets significantly weaken the effective Hubbard interaction between the Ni $3d_{x^2-y^2}$ electrons and help the conventional phonon mechanism? (iv) Can we switch the presence/absence of the additional Fermi pockets?

For these issues, we show the following: (i) We need two orbitals to describe the additional low-energy bands: the Nd $5d_{3z^2-r^2}$ orbital and interstitial s orbital (or the Nd $5d_{xy}$ orbital [31]). (ii) In the three-orbital model for the Ni $3d_{x^2-y^2}$ orbitals and two orbitals in the Nd layer, the hybridization between the Ni and Nd layer is weak; thus, the Ni $3d_{x^2-y^2}$ electrons are almost isolated. (iii) The metallic screening by the Nd layer is not significant, leaving the Ni $3d_{x^2-y^2}$ electrons strongly correlated. On the other hand, the electron-phonon coupling is not sufficiently strong to mediate superconductivity of $T_c \sim 10$ K. (iv) By controlling the hybridization between the interstitial state and the Nd $5d_{xy}$ orbital, we can change the size of the additional Fermi pockets. More specifically, we show that the additional Fermi pockets almost disappear in $\text{NaNd}_2\text{NiO}_4$ and $\text{NaCa}_2\text{NiO}_3$. While the cuprates belong to the charge-transfer type in the Zaanen-Sawatzky-Allen classification [34], these nickelate compounds will provide an interesting playground to investigate the possibility of high- T_c superconductivity in the Mott-Hubbard regime.

The structure of the paper is as follows. After describing the detail of the methods in Sec. II, in Sec. III A we first show the band dispersion and the Bloch wave functions at some specific \mathbf{k} points. We will see that the Fermi surface consists of three bands: the Ni $3d_{x^2-y^2}$ band, Nd $5d_{3z^2-r^2}$ band, and that formed by a bonding state between interstitial and Nd $5d_{xy}$ orbitals in the Nd layer. To exclude the possibility of phonon-mediated superconductivity, we calculate the phonon frequencies and electron-phonon coupling in Sec. III B. We show that the electron-phonon coupling constant is much smaller than 0.5, so that phonons cannot mediate superconductivity of $T_c \sim 10$ K. To consider the possibility of unconventional superconductivity, we then derive an effective low-energy model of NdNiO_2 in Sec. III C. By looking at the tight-binding parameters in the Hamiltonian, and plotting the projected density of states (PDOSs), we show that the hybridization between the Ni $3d_{x^2-y^2}$ state and the Nd-layer states is small. In Sec. III D, we perform a calculation based on the constrained random phase approximation (cRPA) [35], and estimate the interaction parameters in the three-orbital and single-orbital models. By comparing the values of the Hubbard U , we show that the screening effect of the Nd layer on the $3d_{x^2-y^2}$ orbital is not so strong. In Sec. IV, we discuss how we can change the band dispersion and realize an ideal single-component two-dimensional correlated electron system. We show that the hybridization between the interstitial state and the Nd $5d_{xy}$ state is the key parameter for the materials design.

II. METHODS

Here, we describe the calculation methods and conditions used in the following sections.

a. Sections III A, III C, and III D. The DFT band structure calculations for NdNiO_2 are performed using QUANTUM ESPRESSO [36] with the experimental lattice parameters of bulk NdNiO_2 : $a = 3.9208$ Å and $c = 3.2810$ Å [37]. We use Perdew-Burke-Ernzerhof (PBE) [38] norm-conserving pseudopotentials generated by the code ONCVSP (optimized norm-conserving Vanderbilt pseudopotential) [39], which are obtained from the PseudoDojo [40]. We use $11 \times 11 \times 11$ \mathbf{k} points for sampling in the first Brillouin zone. The energy cutoff is set to be 100 Ry for the wave functions, and 400 Ry for the charge density. After the band structure calculations, the maximally localized Wannier functions [41,42] are constructed using RESPACK [43].¹ The three-orbital model consisting of Ni $3d_{x^2-y^2}$, Nd $5d_{3z^2-r^2}$, and interstitial s orbitals is constructed using the outer energy window of $[-2$ eV : 10 eV] and the inner energy window of $[0$ eV : 1.5 eV]. The Ni $3d_{x^2-y^2}$ single-orbital model is constructed using the outer energy window of $[-1.15$ eV : 2.05 eV] without setting the inner energy window. The interaction parameters are calculated with RESPACK [43] using the constrained random-phase approximation (cRPA) method [35], in which we employ the scheme in Ref. [44] for the band disentanglement. The energy cutoff for the dielectric function is set to be 20 Ry. The total number of bands used in the calculation of the polarization is 80, which includes the unoccupied states up to ~ 55 eV with respect to the Fermi level.

To evaluate the effects due to the difference in DFT codes and pseudopotentials, we also derive the low-energy effective models using xTAPP [45]. Although the basic calculation conditions are the same as those of QUANTUM ESPRESSO, the xTAPP calculations employ the pseudopotentials generated as follows: Ni pseudopotential is generated in a slightly ionic semicore $(3s)^2(3p)^6(3d)^9$ configuration by employing the cutoff radii of $r_{3s} = r_{3p} = r_{3d} = 0.8$ bohr. The Nd pseudopotential is constructed under the configuration of $(5s)^2(5p)^6(5d)^1(6s)^2$, while that of the core electrons is $(\text{Kr})(4f)^3$; the $4f$ electrons are frozen and excluded from the pseudopotential. The cutoff radius for the local potential is 1.3 bohr, and those for s , p , d orbitals of the pseudopotential are 1.3, 1.9, and 1.9 bohr, respectively. The $5s$ and $6s$ orbitals share the same cutoff radius. We apply the partial-core correction with a cutoff radius of 1.1 bohr. To stabilize the band calculation under the fairly hard pseudopotential of Ni, the xTAPP calculations adopt the energy cutoffs of 196 and 784 Ry for wave function and the charge density, respectively. With this condition, almost perfect agreement between the QUANTUM ESPRESSO and xTAPP results is obtained for the low-energy band structure and the Wannier function.

b. Section III B. Phonon band structure, electron-phonon coupling constants, and the Eliashberg function of NdNiO_2 are calculated based on density functional perturbation theory

¹Algorithms and applications of RESPACK can be found in Refs. [67–71].

(DFPT) [46], as implemented in QUANTUM ESPRESSO [36]. We use PBE pseudopotentials obtained from the pslibrary 1.0.0 [47]. The $4f$ orbitals of Nd is treated as a frozen core. The kinetic energy cutoff is set to 75 Ry for the wave function and 600 Ry for the charge density. The self-consistent field calculation is conducted with $16 \times 16 \times 16$ \mathbf{k} mesh, and DFPT calculation is performed with $8 \times 8 \times 8$ \mathbf{q} mesh. Before performing DFPT calculation, the lattice constants are optimized until the stress convergence criterion of $|\sigma| < 0.5$ kbar is reached. The optimized values are $a = 3.893$ Å and $c = 3.267$ Å, which reproduce the reported experimental values within 1% error.

c. Section IV. We use Vienna *ab initio* simulation package (VASP) [48] for optimizing the lattice parameters of $\text{LiNd}_2\text{NiO}_4$, $\text{NaNd}_2\text{NiO}_4$, and $\text{NaCa}_2\text{NdO}_3$. The wave-function cutoff energy of 50 Ry is employed along with the PBE PAW potentials [49,50] labeled as Li_{sv} , Na_{pv} , Ca_{sv} , Nd_{3} , Ni_{pv} , and 0. The $12 \times 12 \times 8$ \mathbf{k} mesh is employed for the Brillouin zone sampling. For the calculation of the electronic band structures, we use the *ab initio* code OpenMX [51]. We employ the same \mathbf{k} mesh as that of the VASP calculation. We employ the valence orbital sets $\text{Li}8.0\text{-}s3p3d2$, $\text{Na}9.0\text{-}s3p2d1$, $\text{Ca}9.0\text{-}s4p3d2$, $\text{Nd}8.0\text{-}OC\text{-}s2p2d2f1$, $\text{Ni}6.0\text{H}\text{-}s4p3d2f1$, and $\text{O}5.0\text{-}s3p3d2$. The energy cutoff for the numerical integration is set to 150 Ry.

III. FORMATION OF SINGLE-ORBITAL CORRELATED SYSTEM IN NdNiO_2

A. Band structure

Figure 1(a) shows the DFT band structure for NdNiO_2 . In the calculations, the Nd $4f$ orbitals are assumed to be frozen in the core so that dispersionless $4f$ bands do not appear in the band structure.

We see that the Ni $3d$ bands (located from ~ -3 to ~ 2 eV) and the O $2p$ bands (located from ~ -9 to ~ -3 eV) are well separated, which is in high contrast with the cuprate counterpart CaCuO_2 [29]. Because of the absence of the apical oxygen, the energy level of the Ni $3d_{3z^2-r^2}$ orbital becomes far below the Fermi level. Therefore, as far as the Ni $3d$ orbitals are concerned, only the $3d_{x^2-y^2}$ orbitals form the Fermi surface.

As already pointed out by previous studies [29,30], on top of the Fermi surfaces originated from the Ni $3d_{x^2-y^2}$ orbital, there are additional Fermi pockets around Γ and A points. Around the Γ point, as can be confirmed by the electron density of the Kohn-Sham orbital [Fig. 1(b)], the Fermi pocket originates mainly from the Nd $5d_{3z^2-r^2}$ orbital [29,30]. On the other hand, the orbital character of the Fermi pocket around the A point shows an interesting feature [Fig. 1(c)]. The electron density has a large weight at the interstitial region around $(0, 0, \frac{1}{2})$ site, which corresponds to the site of the apical oxygen in NdNiO_3 . This interstitial state is stabilized because $(0, 0, \frac{1}{2})$ site is surrounded by cations. Therefore, the NdNiO_2 system has a feature similar to electrides where electrons at interstitial regions play a role of anions [53,54]. The interstitial orbitals form a bonding state with the Nd $5d_{xy}$ orbital. The band bottom of the bonding orbital is located at the A point (green open circle below the Fermi level in Fig. 1). The energy

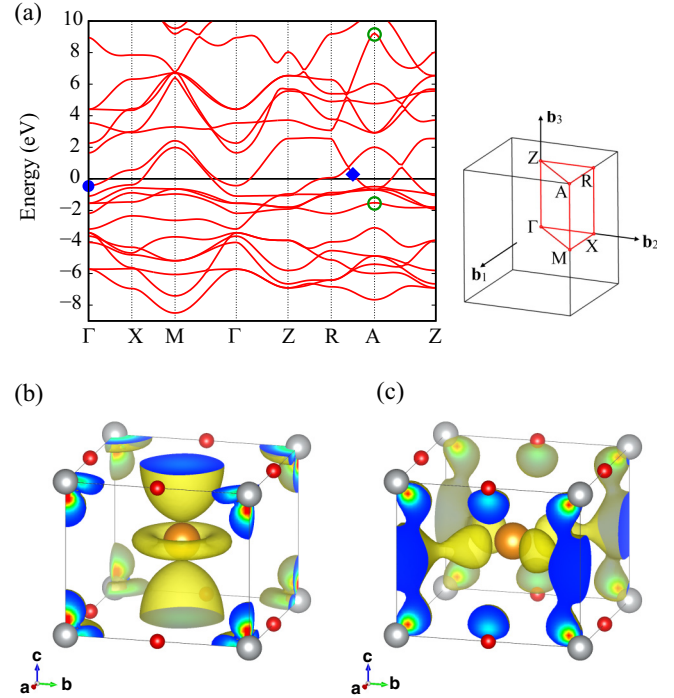


FIG. 1. (a) DFT band structure for NdNiO_2 . The Nd $4f$ orbitals are assumed to be frozen in the core. In NdNiO_2 , the interstitial s and Nd $5d_{xy}$ orbitals form bonding and antibonding states on the $k_z = \pi/c$ plane. The green open circles at the A point indicate the band bottom of the bonding band (below the Fermi level) and the band top of the antibonding band (above the Fermi level). Electron density of the Kohn-Sham states specified by (b) the blue dot at the Γ point and (c) the blue diamond at $(\pi/a, \pi/2a, \pi/c)$ point (drawn by VESTA [52]). The positions of the atoms in the crystal coordinate are follows: Ni $(0, 0, 0)$, Nd $(\frac{1}{2}, \frac{1}{2}, \frac{1}{2})$, O $(\frac{1}{2}, 0, 0)$, O $(0, 0, \frac{1}{2})$.

difference between the bonding and antibonding states at the A point is more than 10 eV. As we will discuss in Sec. IV, we can realize a single-component correlated system by controlling the energy dispersion of the interstitial bonding state.

B. Phonons

Because NdNiO_2 has a different Fermi surface topology from the cuprates, there might be a possibility that the superconducting mechanism is different. One of the most fundamental questions would be whether the observed superconductivity can be explained by the phonon mechanism or not. To investigate this point, we performed phonon calculations and estimated the strength of the electron-phonon coupling.

Figure 2 shows the calculated phonon and electron-phonon properties of NdNiO_2 . The phonon band structure shows no imaginary modes, confirming the dynamical stability of bulk NdNiO_2 . To evaluate the Brillouin-zone-averaged electron-phonon coupling strength λ , we first calculated the coupling strength for each phonon mode ν at momentum \mathbf{q} defined as

$$\lambda_{q\nu} = \frac{2}{N(\epsilon_F)N_k\omega_{q\nu}} \sum_{mnk} |g_{mn,\nu}(\mathbf{k}, \mathbf{q})|^2 \delta(\xi_{mq}) \delta(\xi_{nk+q}).$$

Here, $\omega_{q\nu}$ is the phonon frequency, $N(\epsilon_F)$ is the DOS at the Fermi level, N_k is the number of \mathbf{k} points, $g_{mn,\nu}(\mathbf{k}, \mathbf{q})$ is the

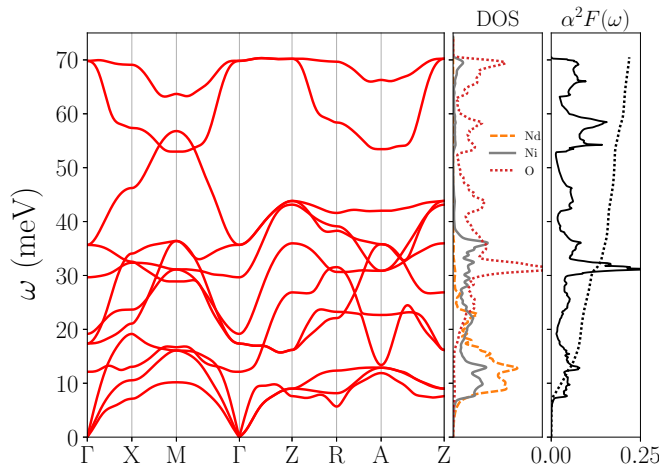


FIG. 2. Phonon band structure (left panel), atom-projected phonon DOS (middle), and the Eliashberg function $\alpha^2 F(\omega)$ (right) of NdNiO₂. The dotted line in the right panel shows the accumulated value of $\lambda(\omega)$ defined as $\lambda(\omega) = 2 \int_0^\omega d\omega' \alpha^2 F(\omega') / \omega'$.

electron-phonon matrix element, and $\xi_{mk} = \epsilon_{mk} - \epsilon_F$ is the energy of the Kohn-Sham orbital m at momentum \mathbf{k} relative to the Fermi level. The double-delta function of $\lambda_{q\nu}$ was evaluated by the Gaussian smearing method with different smearing width σ . We then calculated the Eliashberg function $\alpha^2 F(\omega)$ and λ as $\alpha^2 F(\omega) = \frac{1}{2N_q} \sum_{q\nu} \lambda_{q\nu} \omega_{q\nu} \delta(\omega - \omega_{q\nu})$ and $\lambda = 2 \int_0^\infty d\omega \frac{\alpha^2 F(\omega)}{\omega}$, respectively. The results for $\alpha^2 F(\omega)$ and the accumulated value of λ are shown in the right panel of Fig. 2.

The electron-phonon interaction evaluated with $\sigma = 0.04$ Ry is $\lambda = 0.22$. Although the λ value changes with the smearing width as shown in Table I, we confirmed that it does not reach 0.5 with reasonably small values of σ . We note that the λ values of NdNiO₂ are as small as those calculated for the cuprate superconductors YBa₂Cu₃O₇ ($\lambda = 0.27$, Ref. [55]) and La_{2-x}Sr_xCuO₄ ($\lambda = 0.14$ – 0.22 , Ref. [56]). The logarithmic average of phonon frequencies and the T_c values of NdNiO₂ are also summarized in Table I. The T_c values, obtained using the Allen-Dynes formula [57] with $\mu^* = 0.1$, are too small to account for the experimental results of $T_c = 9$ – 15 K. Therefore, we can rule out the electron-phonon interaction as the exclusive origin of the superconductivity observed in the doped NdNiO₂.

TABLE I. Electron-phonon interaction λ and the logarithmic average of phonon frequencies calculated for NdNiO₂ with different width of the Gaussian smearing. The T_c values are evaluated using the Allen-Dynes formula with $\mu^* = 0.1$.

Smearing width (Ry)	λ	ω_{ln} (K)	T_c (K)
0.04	0.22	283	0.00
0.06	0.28	258	0.06
0.08	0.32	249	0.24

C. Minimal tight-binding Hamiltonian

In Sec. III B, we have seen that the electron-phonon coupling is not strong enough to explain the experimental transition temperature. Next, we consider the possibility of whether the Ni 3d electron systems can be a playground for unconventional superconductivity. To analyze the electron correlation effect, it is essential to derive realistic tight-binding Hamiltonian for the low-energy electrons near the Fermi level [58,59]. Here, as a minimal tight-binding model to reproduce the band structure around the Fermi level, based on the orbital character analysis in Figs. 1(b) and 1(c), we propose a three-orbital model consisting of the Ni 3d_{x²-y²} orbital, Nd 5d_{3z²-r²} orbital, and interstitial *s* orbital centered at (0, 0, $\frac{1}{2}$) site.

Figure 3(a) shows a comparison between the original DFT band structure (red solid curves) and the band dispersion obtained from the three-orbital tight-binding model (blue dashed curves). We see that the band structure near the Fermi level is accurately reproduced. Figure 3(b) visualizes the constructed maximally localized Wannier functions, in which we see that the Wannier functions have characters of Ni 3d_{x²-y²}, Nd 5d_{3z²-r²}, and interstitial *s*, respectively. The Ni 3d_{x²-y²} Wannier orbital has tails of O 2*p* orbitals and forms the antibonding orbital. Similarly, the interstitial *s* orbital has an antibonding character with the Ni 3d_{3z²-r²} orbital. It should be noted that the lobes of the Nd 5d_{xy} orbital with $(\pi/a, \pi/a)$ phase on the *x*-*y* plane [then the phases of the lobes from Nd 5d_{xy} orbitals at (0, 0, $\frac{1}{2}$), (1, 0, $\frac{1}{2}$), (0, 1, $\frac{1}{2}$), (1, 1, $\frac{1}{2}$) sites are aligned] participate in the interstitial *s* Wannier orbital and form the bonding state. This is the reason why the additional Fermi pocket around the A point [$\mathbf{k} = (\pi/a, \pi/a, \pi/c)$] can be described by the interstitial-*s*-centered bonding orbital or Nd-5d_{xy}-centered bonding orbital. See Appendix B for the construction of another three-orbital model using the Nd-5d_{xy}-centered bonding orbital [31].

We show the calculated density of states (DOS) for the three-orbital model and the decomposition into the three orbitals [Ni 3d_{x²-y²} (red), Nd 5d_{3z²-r²} (green), and the interstitial *s* (blue)] in Fig. 3(c), and the fat bands (bands weighted by the orbital components) in Fig. 3(d). Notably, the hybridization between the Ni 3d_{x²-y²} orbital and the other orbitals is negligibly small and the Ni 3d_{x²-y²} orbital form an isolated single band. From the symmetry consideration, we can show that the transfer between the neighboring Ni 3d_{x²-y²} and Nd 5d_{3z²-r²} orbitals is zero. The same is true for the transfer between the neighboring Ni 3d_{x²-y²} and interstitial *s* orbitals. These facts and a large difference in the onsite level between the Ni 3d_{x²-y²} and Nd 5d_{3z²-r²} and the interstitial *s* orbitals (about 2.6 and 2.4 eV, respectively) help the isolation of the Ni 3d_{x²-y²} orbital.

We see that at the Fermi level, the majority of the DOS is from the Ni 3d_{x²-y²} orbital, but both the Nd 5d_{3z²-r²} and the interstitial *s* orbitals also have finite DOS. The additional Fermi surface around the Γ point is formed by the Nd 5d_{3z²-r²} orbital, whereas that around the A point is formed by the interstitial *s* orbital, in accord with the orbital character analysis in Figs. 1(b) and 1(c). The absence of the apical oxygen makes the lattice constant along the *z* direction small, resulting in the large bandwidth of the Nd-layer orbitals. Because of the finite occupation of the Nd 5d_{3z²-r²} and the interstitial *s* orbitals, the

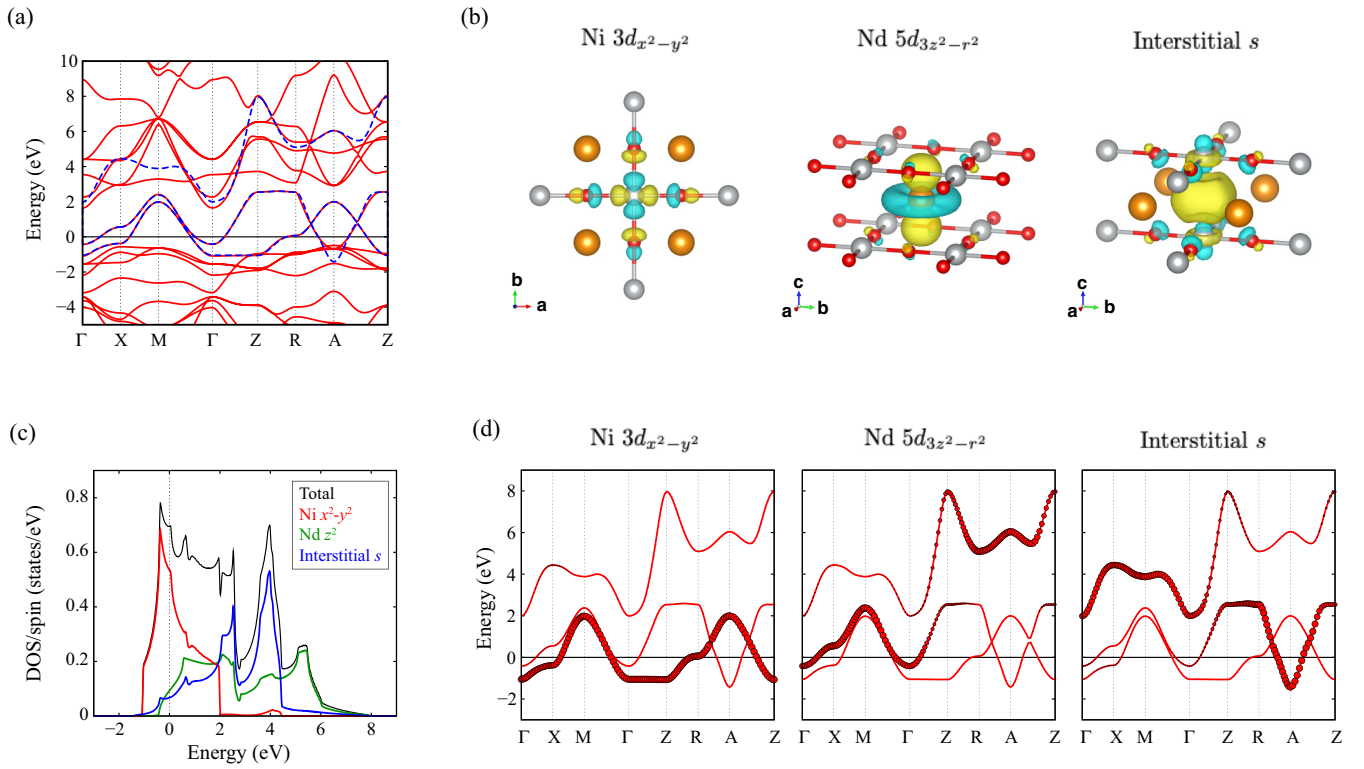


FIG. 3. (a) Dispersion of the three-orbital tight-binding model (blue dashed curves). Red solid curves show the DFT band structure. (b) Isosurfaces (yellow: positive, light blue: negative) of constructed maximally localized Wannier functions (drawn by VESTA [52]). (c) Projected density of states (PDOS) and (d) fat bands of the three-orbital tight-binding model. In the fat bands, the size of the symbols is proportional to the weight of the respective orbital components.

occupation of the Ni $3d_{x^2-y^2}$ orbital deviates from half-filling. The calculated occupation is about 0.87, corresponding to 13% hole doping. This number is consistent with an estimate in the previous study [29].

The absence of apical oxygen makes the Ni $3d_{x^2-y^2}$ band highly two dimensional. It can be confirmed by the shape of the PDOS of Ni $3d_{x^2-y^2}$ and the negligible dispersion along the z direction.

D. Correlation strength

The analysis in Sec. III C leads to the conclusion that the low-energy electronic structure of NdNiO₂ is well characterized by the highly two-dimensional Ni $3d_{x^2-y^2}$ band and two independent Nd-layer bands. Then, an important question is whether Ni $3d_{x^2-y^2}$ bands are strongly correlated or not. To answer this question, we estimate the strength of the effective Coulomb repulsion using the cRPA method [35].

First, we calculate the interaction parameters for the three-orbital model. Table II shows our calculated effective interaction parameters of the three-orbital model. The Ni $3d_{x^2-y^2}$ onsite interaction U is about 3.1 eV, which is comparable to the bandwidth of the Ni $3d_{x^2-y^2}$ band (about 3 eV). Compared to U for the Ni $3d_{x^2-y^2}$ orbital, U for the Nd $5d_{3z^2-r^2}$ and the interstitial s orbitals are smaller, reflecting their larger spatial spread.

If we take account of the metallic screening by the Nd-layer orbitals, the effective interaction parameter for the Ni $3d_{x^2-y^2}$ orbital will be reduced. To investigate this screening effect, we

calculate the interaction parameter for the Ni $3d_{x^2-y^2}$ single-orbital model by including the Nd-layer screening effect. Table III shows the main Coulomb interaction parameters of the single-band model. We also show the hopping parameters in the table. What is interesting is that even when the Nd-layer metallic screening effect is incorporated, the Ni $3d_{x^2-y^2}$ orbital has an onsite interaction of about 2.6 eV, and the reduction of U is less than 20%. We note that if the Ni $3d_{x^2-y^2}$ intraband metallic screening effect is further taken into account, U is drastically reduced down to about 1.2 eV. Therefore, the effect of the metallic screening by electrons in the Nd layer on the Ni $3d_{x^2-y^2}$ onsite interaction is weak.

The mechanism behind the weak screening effect is summarized by the following three points: (i) The electron density of the Nd-layer orbitals is spatially separated from the NiO₂ plane. Therefore, the electron clouds of the Nd-layer orbitals cannot directly screen the Coulomb interaction in the NiO₂ plane. (ii) The Nd-layer polarization is not strong because

TABLE II. Calculated onsite interaction parameters U in the three-orbital model. Unit is given in eV. QUANTUM ESPRESSO and xTAPP give consistent results.

	QUANTUM ESPRESSO	xTAPP
$U_{\text{Ni}(3d_{x^2-y^2})}$	3.109	3.129
$U_{\text{Nd}(5d_{z^2})}$	2.108	2.133
$U_{\text{interstitial}(s)}$	1.075	1.121

TABLE III. Calculated interaction parameters in the single-orbital model. U is onsite interaction and V_a and V_c represent nearest-neighbor interactions along the a and c axes, respectively. t , t' , t'' are the nearest, next-nearest, and third-nearest transfer integrals, respectively. Unit is given in eV. QUANTUM ESPRESSO and xTAPP give consistent results.

	QUANTUM ESPRESSO	xTAPP
U	2.608	2.578
V_a	0.218	0.223
V_c	0.143	0.154
t	-0.370	-0.375
t'	0.092	0.091
t''	-0.045	-0.044
$ U/t $	7.052	6.874
t'/t	-0.250	-0.243

the DOS of the Nd-layer orbitals is small at the Fermi level. (iii) The orbital off-diagonal polarization involving the Ni $3d_{x^2-y^2}$ orbital and the Nd-layer orbitals is small because of the tiny hybridization as discussed in the previous section. More detailed discussion on the role of the Nd-layer screening can be found in Appendix A.

Therefore, the Ni $3d_{x^2-y^2}$ orbital feels strong onsite Coulomb repulsion. The nearest transfer t is nearly -0.37 eV, and thus the ratio $|U/t|$ amounts to around 7, whose value is comparable to that estimated for the cuprates [60–65]. Therefore, we conclude that the Ni $3d_{x^2-y^2}$ electrons in NdNiO₂ form strongly correlated two-dimensional system.

As for other parameters in the table, V_a and V_c represent nearest-neighbor interactions along the a and c axes, respectively, which are sufficiently smaller than U . t' and t'' are the next-nearest and third-nearest transfer integrals, respectively. In particular, frustration degree of freedom in the square lattice t'/t is nearly -0.25 , which is comparable to that of cuprate [29,66]

IV. BAND ENGINEERING FOR REALIZING PURE MOTT-HUBBARD-TYPE SINGLE-BAND SYSTEM

So far, we have shown that the electronic structure of NdNiO₂ can be accurately described by a single-orbital strongly correlated Ni $3d_{x^2-y^2}$ band coupled weakly to the Nd-layer electrons. Considering the large charge-transfer energy, NdNiO₂ would belong to the Mott-Hubbard type [32] rather than the charge-transfer type in the Zaanen-Sawatzky-Allen classification scheme [34]. Therefore, the nickelate would be an interesting playground for investigating superconductivity in the Mott-Hubbard-type single-band system, which will promote the understanding of the high- T_c superconductivity in the cuprates.

Here, we propose a way to perform “band engineering” to realize a more ideal two-dimensional Mott-Hubbard-type single-band system, in which almost only the Ni $3d_{x^2-y^2}$ band intersects the Fermi surface. For this purpose, we need to eliminate the Fermi pocket around Γ and A points originated from the Nd-layer band. Because the Fermi pocket around the Γ point is already small, we hereafter focus on the Fermi pocket around the A point.

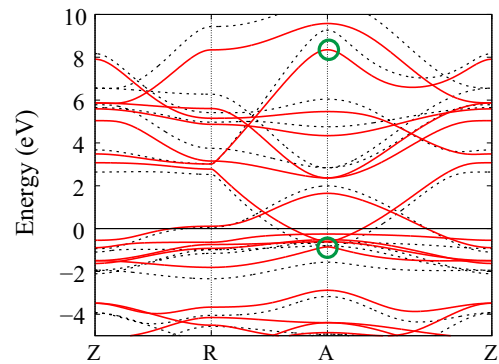


FIG. 4. DFT band structure of NdNiO₂. The black dotted and red solid curves are calculated with the original lattice constant a and $1.05 \times a$, respectively. The green open circles indicate the band bottom of the bonding band between the interstitial s and Nd $5d_{xy}$ orbitals (below the Fermi level) and the band top of the antibonding band (above the Fermi level).

As we have already discussed in Sec. III A, the band dispersion of the bonding state between the interstitial s and Nd $5d_{xy}$ orbitals takes its minimum at the A point in k space.² The energy of the band bottom is located well below the Fermi level (~ -1.5 eV). The energy of the antibonding state at the A point is located around 9 eV, and the energy difference is larger than 10 eV (see Fig. 1).

In order to eliminate the Fermi pocket from the bonding orbital, there are basically two strategies: (i) reduce the bandwidth and make the energy difference between the bonding and antibonding states smaller; (ii) raise the energy center of the bonding-antibonding gap. The former is related to the strength of the hopping between the interstitial s and Nd $5d_{xy}$ orbitals, whereas the latter is related to their onsite energy levels. Because the hopping amplitude is easier to control, we follow the former strategy.

To reduce the hopping amplitude between the interstitial s and Nd $5d_{xy}$ orbitals, the simplest way is to increase the in-plane lattice constant a . By increasing a by 5%, we indeed see that the energy difference between the bonding and antibonding states at the A point becomes smaller and that the band bottom of the bonding state becomes closer to the Fermi level (see Fig. 4). However, the effect is not strong enough to eliminate the Fermi surface.

Alternatively, let us introduce a new block anion layer, then we can reduce the hopping amplitude without applying the tensile strain. Here, the unit cell consists of two anion layers (NiO₂ and new anion layer) and two cation layers (such as La and Nd). It should be noted that the mirror inversion symmetry with respect to the cation layers is broken. Then, the height of the center of the interstitial s and cation $5d_{xy}$ orbitals becomes

²We note that on $k_z = 0$ plane, the interstitial s and Nd $5d_{xy}$ orbitals can also hybridize to Ni $3d_{3z^2-r^2}$ orbital, whereas on $k_z = \pi/c$ plane, the hybridization is zero by symmetry. This makes a difference between $k_z = 0$ and $k_z = \pi/c$ planes, where the former has no Fermi pocket around M point while the latter has the Fermi pocket around the A point.

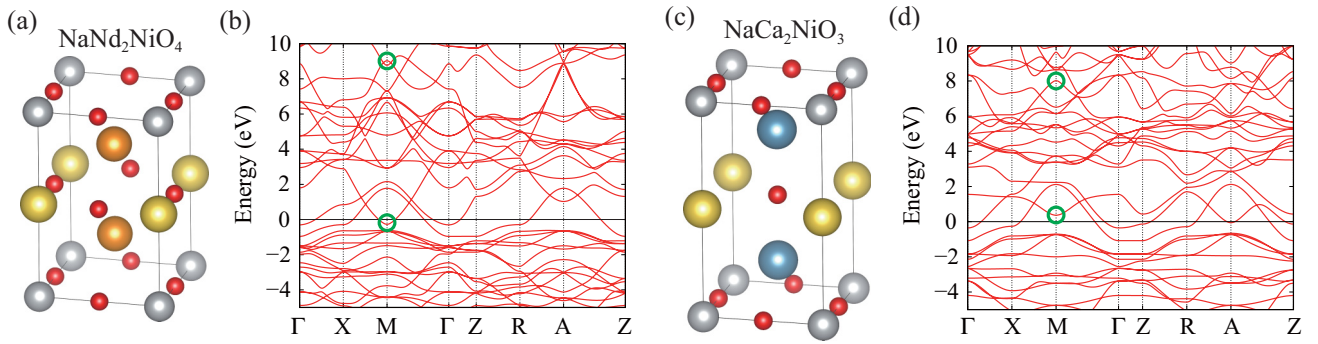


FIG. 5. (a) Crystal structure and (b) DFT band structure of $\text{NaNd}_2\text{NiO}_4$. (c) Crystal structure and (d) DFT band structure of $\text{NaCa}_2\text{NiO}_3$. The green open circles indicate the band bottom of the bonding band between the interstitial s and cation d_{xy} orbital (below the Fermi level) and the band top of the antibonding band (above the Fermi level).

different. Because of the bending of the hopping path, the hopping amplitude is expected to decrease.

We have verified several different possibilities for the new block layers, such as LiO_2 , NaO_2 , LiO , and NaO . In the case of LiO and NaO , to satisfy the charge neutrality, we change the cation layer from Nd to Sr or Ca . Among them, we find that $\text{NaNd}_2\text{NiO}_4$ and $\text{NaCa}_2\text{NiO}_3$, whose structures are shown in Figs. 5(a) and 5(c), are potential candidates to realize an ideal two-dimensional Mott-Hubbard-type correlated system. The band structures for $\text{NaNd}_2\text{NiO}_4$ and $\text{NaCa}_2\text{NiO}_3$ are shown in Figs. 5(b) and 5(d), respectively. In these materials, because there exist two anion layers, M point corresponds to A point in NdNiO_2 . Remarkably, in both materials, the Fermi pockets around the M point almost disappear.

Indeed, in these two materials, as shown in Table IV, the energy difference between the bonding and antibonding states ΔE_{ba} (9.298 and 7.650 eV) is significantly smaller than that of NdNiO_2 (10.837 eV). Especially in $\text{NaCa}_2\text{NiO}_3$, even though the in-plane lattice constant a is smaller than that of NdNiO_2 , we see a significant decrease in ΔE_{ba} , which can be ascribed to the bending of the hopping path on the cation layer. The increase in the energy difference between the interstitial s and

$\text{Nd } 5d_{xy}$ orbitals (see ΔE_{sd}) makes the hybridization smaller, and this is also helpful in reducing ΔE_{ba} . Finally, let us mention that the effect is material dependent. For example, in $\text{LiNd}_2\text{NiO}_4$, the decrease in ΔE_{ba} is not so drastic and the Fermi pocket survives (not shown). However, we see that the decrease in ΔE_{ba} is a general tendency, therefore, we believe that the present results provide a useful guideline for future material synthesis.

V. SUMMARY

In this paper, we studied the role of the states in the Nd layer in the newly discovered nickelate superconductor NdNiO_2 . While only the $3d_{x^2-y^2}$ band among the five $3d$ bands intersects the Fermi level, we need at least two states to represent the Fermi pockets formed by the states in the Nd layer: one is the $\text{Nd } 5d_{3z^2-y^2}$ state, and the other is an interstitial s state, which makes the situation similar to electrides. In the three-orbital model for these states, the hybridization between the Nd -layer states and $\text{Ni } 3d_{x^2-y^2}$ state is small. We performed a calculation based on the cRPA to estimate the interaction parameters. By comparing the results for the three-orbital and single-orbital models for the $\text{Ni } 3d_{x^2-y^2}$ orbital, we found that the screening effect of the Nd -layer states is not so effective, reducing the Hubbard U between the $\text{Ni } 3d_{x^2-y^2}$ electrons just by 10%–20%. On the other hand, the electron-phonon coupling constant is not larger than 0.5, so that the phonon mechanism is unlikely. Given the results indicating that NdNiO_2 hosts an almost ideal single-component correlated $3d_{x^2-y^2}$ electron, we further study whether we can eliminate the Fermi pockets formed by the Nd -layer states. We found that these Fermi pockets dramatically shrink if the hybridization between the interstitial s state and the $\text{Nd } 5d_{xy}$ states is reduced. By an extensive materials search, we found that the Fermi pockets almost disappear in $\text{NaNd}_2\text{NiO}_4$ and $\text{NaCa}_2\text{NiO}_3$. These nickelates will provide an interesting playground to investigate the possibility of high- T_c superconductivity in the Mott-Hubbard regime.

ACKNOWLEDGMENTS

We acknowledge the financial support of JSPS Kakenhi Grants No. 16H06345 (Y.N., M.H., T.T., Y.Y., K.N., and

TABLE IV. Energy of the interstitial s and the cation d_{xy} orbitals (ΔE_s and $\Delta E_{d_{xy}}$, respectively) for NdNiO_2 , $\text{LiNd}_2\text{NiO}_4$, $\text{NaNd}_2\text{NiO}_4$, and $\text{NaCa}_2\text{NiO}_3$. We also show the energies for the bottom of the bonding band E_b and the top of the antibonding band E_a . ΔE_{sd} and ΔE_{ba} are the energy difference between s and d_{xy} states and bonding and antibonding bands, respectively. Here, d_{xy} indicates the $\text{Nd } 5d_{xy}$ orbital for NdNiO_2 , $\text{LiNd}_2\text{NiO}_4$, and $\text{NaNd}_2\text{NiO}_4$, and the $\text{Ca } 3d_{xy}$ orbital for $\text{NaCa}_2\text{NiO}_3$. E_s and $E_{d_{xy}}$ are estimated, respectively, from R and Z points in NdNiO_2 , and from X and Γ points in the other materials. In these \mathbf{k} points, the hybridization between the interstitial s or d_{xy} orbitals and the other orbitals becomes small. E_b and E_a are estimated from A point in NdNiO_2 , and M point in the other materials. The unit for length is \AA . The energy unit is eV.

	a	E_s	$E_{d_{xy}}$	E_b	E_a	ΔE_{sd}	ΔE_{ba}
NdNiO_2	3.921 (expt.)	2.529	3.676	-1.567	9.270	1.147	10.837
$\text{LiNd}_2\text{NiO}_4$	3.908	3.116	4.212	-1.014	9.545	1.096	10.559
$\text{NaNd}_2\text{NiO}_4$	4.056	3.739	3.908	-0.271	9.027	0.169	9.298
$\text{NaCa}_2\text{NiO}_3$	3.918	1.421	4.777	0.368	8.018	3.356	7.650

TABLE V. Comparison of cRPA onsite interactions among seven-orbital, five-orbital, three-orbital, and single-orbital models. Unit is given in eV. QUANTUM ESPRESSO and xTAPP give consistent results.

	QUANTUM ESPRESSO				xTAPP			
	7 orbital	5 orbital	3 orbital	1 orbital	7 orbital	5 orbital	3 orbital	1 orbital
$U_{\text{Ni}(3d_{x^2-y^2})}$	5.112	2.933	3.109	2.608	5.144	2.841	3.129	2.578
$U_{\text{Ni}(3d_{z^2})}$	6.824	2.649			6.757	2.793		
$U_{\text{Ni}(3d_{xy})}$	5.501	3.294			5.488	3.171		
$U_{\text{Ni}(3d_{yz})}$	5.841	3.096			5.837	3.099		
$U_{\text{Ni}(3d_{zx})}$	5.841	3.096			5.837	3.099		
$U_{\text{Nd}(5d_{z^2})}$	2.972		2.108		2.950		2.134	
$U_{\text{interstitial}(s)}$	2.491		1.075		2.453		1.121	

R.A.), No. 17K14336 (Y.N.), No. 18H01158 (Y.N.), No. 16K05452 (K.N.), No. 17H03393 (K.N.), No. 17H03379 (K.N.), No. 19K03673 (K.N.), and No. 19H05825 (R.A.).

APPENDIX A: SCREENING PROCESS FOR THE ONSITE INTERACTION OF Ni $3d_{x^2-y^2}$ ORBITAL

In Sec. III D, we have discussed that as far as the three-orbital model is concerned, the screening effect of the Nd layer on the NiO₂ layer is not so appreciable. In this Appendix, we discuss this point in more detail by comparing different models including five Ni $3d$ orbitals.

Table V is a list of calculated cRPA onsite interactions for the seven-orbital, five-orbital, three-orbital, and single-orbital models. In the seven-orbital model, the five Ni $3d$ orbitals, Nd $5d_{3z^2-r^2}$, and interstitial s orbitals are considered. In the five-orbital model, only the five Ni $3d$ orbitals are taken into account.

Here, we focus on the onsite interaction U of the Ni $3d_{x^2-y^2}$ orbital. In the calculation of U using the cRPA, the screening processes within the orbitals included in the model are excluded in order to avoid the double counting of the screening [35]. Therefore, the U value is different among different models because the exclusion of the screening is done in a different way. The comparison of the onsite interaction parameters shows the following:

(1) The difference in U between the seven-orbital and five-orbital models is mainly due to screening through the Nd layer [types (b) and (c) in Fig. 6], which is excluded in the calculation of U in the seven-orbital model. For example, since Ni $3d_{3z^2-r^2}$ orbitals can hybridize with the interstitial s orbital in the Nd layer, the screening channel shown in the Fig. 6(b) can be active. Then, the screening from the Nd layer becomes effective, in accord with the recent cRPA calculation by Sakakibara *et al.* [31].

(2) The difference in U between the seven-orbital and three-orbital models is mainly due to screening through the NiO₂ layer [Fig. 6(a)] and partially contributed from the Nd-layer screening [Fig. 6(b)].

(3) The difference in U between the three-orbital and single-orbital models arises from the screening process in Fig. 6(c) only. It should be noted here that the DOS of the Nd-layer orbitals is small at the Fermi level [Fig. 3(c)], and then this screening channel can not be drastic [point (ii) in Sec. III D]. In addition, the process in Fig. 6(b) becomes almost irrelevant because the hybridization between the Ni $3d_{x^2-y^2}$ orbital and the Nd $5d_{3z^2-r^2}$ and interstitial s orbitals is negligibly small [point (iii) in Sec. III D]. The process in Fig. 6(a) is also irrelevant because the screening process from the Ni $3d_{x^2-y^2}$ orbital itself is excluded in the cRPA [point (i) in Sec. III D].

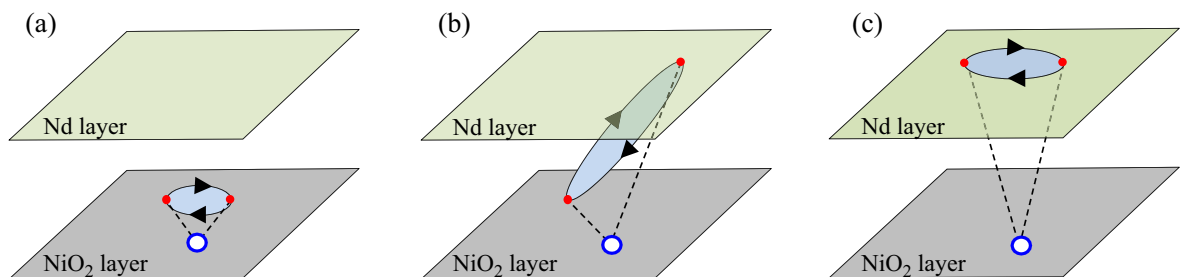


FIG. 6. Schematic diagram for screening processes for the $3d_{x^2-y^2}$ orbital at a Ni site (blue circles). Upper-green and lower-gray layers represent Nd and NiO₂ layers, respectively. Dashed lines are Coulomb interactions, and solid oval lines with arrows describe the polarization in which the red dots represent the polarization points. In the figure, an RPA diagram (symbolically for the second-order one) for the effective onsite interaction is shown, and three types of screening processes are depicted. (a) Screening process via the intralayer polarization in the NiO₂ layer. (b) Screening process via the interlayer polarization. (c) Screening process via the intralayer polarization in Nd layer. The red points and the blue circles in (a) and (b) may share the same Ni site, although they are depicted at difference positions.

Therefore, whereas the Nd-layer screening plays an important role in the seven-orbital model [31], its effect is small in the three-orbital model.

APPENDIX B: THREE-ORBITAL MODEL WITH THE Nd $5d_{xy}$ ORBITAL

As we have already discussed in Sec. III C, the DFT band dispersion around the A point can also be reproduced by constructing the model with the Nd $5d_{xy}$ orbital. For comparison, we show, in Fig. 7, the calculated band dispersion of this alternative three-orbital tight-binding Hamiltonian [Fig. 7(a)] and the resulting maximally localized Wannier function for Nd $5d_{xy}$ orbital [Fig. 7(b)]. Compared with the Wannier-interpolated band in Fig. 3(a), we see differences in the dispersion of the conduction band.

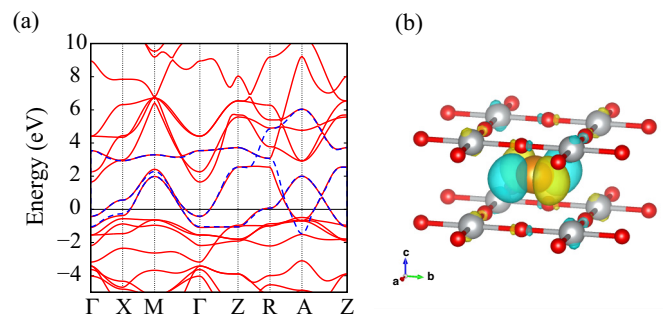


FIG. 7. (a) Dispersion of three-orbital tight-binding model using Ni $3d_{x^2-y^2}$, Nd $5d_{3z^2-r^2}$, and Nd $5d_{xy}$ orbitals (blue dashed curves). Red solid curves show the DFT band structure. (b) Isosurfaces (yellow: positive, light blue: negative) of constructed maximally localized Wannier function for Nd $5d_{xy}$ orbital (drawn by VESTA [52]).

- [1] J. G. Bednorz and K. A. Müller, Possible high T_c superconductivity in the Ba-La-Cu-O system, *Z. Phys. B: Condens. Matter* **64**, 189 (1986).
- [2] G. R. Stewart, Unconventional superconductivity, *Adv. Phys.* **66**, 75 (2017).
- [3] R. Arita, K. Kuroki, and H. Aoki, Spin-fluctuation exchange study of superconductivity in two- and three-dimensional single-band Hubbard models, *Phys. Rev. B* **60**, 14585 (1999).
- [4] R. Arita, K. Kuroki, and H. Aoki, d- and p-wave superconductivity mediated by spin fluctuations in two- and three-dimensional single-band repulsive Hubbard model, *J. Phys. Soc. Jpn.* **69**, 1181 (2000).
- [5] P. Monthoux and G. G. Lonzarich, p -wave and d-wave superconductivity in quasi-two-dimensional metals, *Phys. Rev. B* **59**, 14598 (1999).
- [6] P. Monthoux and G. G. Lonzarich, Magnetically mediated superconductivity in quasi-two and three dimensions, *Phys. Rev. B* **63**, 054529 (2001).
- [7] H. Sakakibara, H. Usui, K. Kuroki, R. Arita, and H. Aoki, Two-Orbital Model Explains the Higher Transition Temperature of the Single-Layer Hg-Cuprate Superconductor Compared to That of the La-Cuprate Superconductor, *Phys. Rev. Lett.* **105**, 057003 (2010).
- [8] H. Sakakibara, K. Suzuki, H. Usui, K. Kuroki, R. Arita, D. J. Scalapino, and H. Aoki, Multiorbital analysis of the effects of uniaxial and hydrostatic pressure on T_c in the single-layered cuprate superconductors, *Phys. Rev. B* **86**, 134520 (2012).
- [9] H. Sakakibara, H. Usui, K. Kuroki, R. Arita, and H. Aoki, Origin of the material dependence of T_c in the single-layered cuprates, *Phys. Rev. B* **85**, 064501 (2012).
- [10] M. R. Norman, Materials design for new superconductors, *Rep. Prog. Phys.* **79**, 074502 (2016).
- [11] W. Pickett, D. Singh, D. Papaconstantopoulos, H. Krakauer, M. Cyrot, and F. Cyrot-Lackmann, Theoretical studies of Sr_2VO_4 , a charge conjugate analog of La_2CuO_4 , *Phys. C (Amsterdam)* **162-164**, 1433 (1989).
- [12] Y. Imai, I. Solovyev, and M. Imada, Electronic Structure of Strongly Correlated Systems Emerging from Combining Path-Integral Renormalization Group with the Density-Functional Approach, *Phys. Rev. Lett.* **95**, 176405 (2005).
- [13] J. Matsuno, Y. Okimoto, M. Kawasaki, and Y. Tokura, Variation of the Electronic Structure in Systematically Synthesized Sr_2MO_4 ($M = \text{Ti, V, Cr, Mn, and Co}$), *Phys. Rev. Lett.* **95**, 176404 (2005).
- [14] R. Arita, A. Yamasaki, K. Held, J. Matsuno, and K. Kuroki, Sr_2VO_4 and Ba_2VO_4 under pressure: An orbital switch and potential d^1 superconductor, *Phys. Rev. B* **75**, 174521 (2007).
- [15] J. Chaloupka and G. Khaliullin, Orbital Order and Possible Superconductivity in $\text{LaNiO}_3/\text{LaMO}_3$ Superlattices, *Phys. Rev. Lett.* **100**, 016404 (2008).
- [16] P. Hansmann, X. Yang, A. Toschi, G. Khaliullin, O. K. Andersen, and K. Held, Turning a Nickelate Fermi Surface into a Cupratelike One through Heterostructuring, *Phys. Rev. Lett.* **103**, 016401 (2009).
- [17] P. Hansmann, A. Toschi, X. Yang, O. K. Andersen, and K. Held, Electronic structure of nickelates: From two-dimensional heterostructures to three-dimensional bulk materials, *Phys. Rev. B* **82**, 235123 (2010).
- [18] M. J. Han, X. Wang, C. A. Marianetti, and A. J. Millis, Dynamical Mean-Field Theory of Nickelate Superlattices, *Phys. Rev. Lett.* **107**, 206804 (2011).
- [19] B. J. Kim, H. Jin, S. J. Moon, J.-Y. Kim, B.-G. Park, C. S. Leem, J. Yu, T. W. Noh, C. Kim, S.-J. Oh, J.-H. Park, V. Durairaj, G. Cao, and E. Rotenberg, Novel $J_{\text{eff}} = 1/2$ Mott State Induced by Relativistic Spin-Orbit Coupling in Sr_2IrO_4 , *Phys. Rev. Lett.* **101**, 076402 (2008).
- [20] B. J. Kim, H. Ohsumi, T. Komesu, S. Sakai, T. Morita, H. Takagi, and T. Arima, Phase-sensitive observation of a spin-orbital Mott state in Sr_2IrO_4 , *Science* **323**, 1329 (2009).
- [21] H. Watanabe, T. Shirakawa, and S. Yunoki, Microscopic Study of a Spin-Orbit-Induced Mott Insulator in Ir Oxides, *Phys. Rev. Lett.* **105**, 216410 (2010).
- [22] H. Watanabe, T. Shirakawa, and S. Yunoki, Monte Carlo Study of an Unconventional Superconducting Phase in Iridium Oxide $J_{\text{eff}} = 1/2$ Mott Insulators Induced by Carrier Doping, *Phys. Rev. Lett.* **110**, 027002 (2013).

- [23] Y. K. Kim, N. H. Sung, J. D. Denlinger, and B. J. Kim, Observation of a d-wave gap in electron-doped Sr_2IrO_4 , *Nat. Phys.* **12**, 37 (2015).
- [24] Y. J. Yan, M. Q. Ren, H. C. Xu, B. P. Xie, R. Tao, H. Y. Choi, N. Lee, Y. J. Choi, T. Zhang, and D. L. Feng, Electron-Doped Sr_2IrO_4 : An Analogue of Hole-Doped Cuprate Superconductors Demonstrated by Scanning Tunneling Microscopy, *Phys. Rev. X* **5**, 041018 (2015).
- [25] R. Arita, J. Kuneš, A. V. Kozhevnikov, A. G. Eguiluz, and M. Imada, Ab initio Studies on the Interplay between Spin-Orbit Interaction and Coulomb Correlation in Sr_2IrO_4 and Ba_2IrO_4 , *Phys. Rev. Lett.* **108**, 086403 (2012).
- [26] C. Martins, M. Aichhorn, L. Vaugier, and S. Biermann, Reduced Effective Spin-Orbital Degeneracy and Spin-Orbital Ordering in Paramagnetic Transition-Metal Oxides: Sr_2IrO_4 versus Sr_2RhO_4 , *Phys. Rev. Lett.* **107**, 266404 (2011).
- [27] D. Li, K. Lee, B. Y. Wang, M. Osada, S. Crossley, H. R. Lee, Y. Cui, Y. Hikita, and H. Y. Hwang, Superconductivity in an infinite-layer nickelate, *Nature (London)* **572**, 624 (2019).
- [28] M. Azuma, Z. Hiroi, M. Takano, Y. Bando, and Y. Takeda, Superconductivity at 110 K in the infinite-layer compound $(\text{Sr}_{1-x}\text{Ca}_x)_{1-y}\text{CuO}_2$, *Nature (London)* **356**, 775 (1992).
- [29] A. S. Botana and M. R. Norman, Similarities and differences between infinite-layer nickelates and cuprates and implications for superconductivity, [arXiv:1908.10946](https://arxiv.org/abs/1908.10946).
- [30] K.-W. Lee and W. E. Pickett, Infinite-layer LaNiO_2 : Ni^{1+} is not Cu^{2+} , *Phys. Rev. B* **70**, 165109 (2004).
- [31] H. Sakakibara, H. Usui, K. Suzuki, T. Kotani, H. Aoki, and K. Kuroki, Model construction and a possibility of cuprate-like pairing in a new d^9 nickelate superconductor $(\text{Nd,Sr})\text{NiO}_2$, [arXiv:1909.00060](https://arxiv.org/abs/1909.00060).
- [32] M. Jiang, M. Berciu, and G. A. Sawatzky, Doped holes in NdNiO_2 and high- T_c cuprates show little similarity, [arXiv:1909.02557](https://arxiv.org/abs/1909.02557).
- [33] X. Wu, D. Di Sante, T. Schwemmer, W. Hanke, H. Y. Hwang, S. Raghu, and R. Thomale, Robust $d_{x^2-y^2}$ -wave superconductivity of infinite-layer nickelates, [arXiv:1909.03015](https://arxiv.org/abs/1909.03015).
- [34] J. Zaanen, G. A. Sawatzky, and J. W. Allen, Band Gaps and Electronic Structure of Transition-Metal Compounds, *Phys. Rev. Lett.* **55**, 418 (1985).
- [35] F. Aryasetiawan, M. Imada, A. Georges, G. Kotliar, S. Biermann, and A. I. Lichtenstein, Frequency-dependent local interactions and low-energy effective models from electronic structure calculations, *Phys. Rev. B* **70**, 195104 (2004).
- [36] P. Giannozzi, O. Andreussi, T. Brumme, O. Bunau, M. B. Nardelli, M. Calandra, R. Car, C. Cavazzoni, D. Ceresoli, M. Cococcioni, N. Colonna, I. Carnimeo, A. D. Corso, S. de Gironcoli, P. Delugas, R. A. DiStasio, Jr., A. Ferretti, A. Floris, G. Fratesi, G. Fugallo *et al.*, Advanced capabilities for materials modeling with QUANTUM ESPRESSO, *J. Phys.: Condens. Matter* **29**, 465901 (2017).
- [37] M. Hayward and M. Rosseinsky, Synthesis of the infinite layer Ni(I) phase NdNiO_{2+x} by low temperature reduction of NdNiO_3 with sodium hydride, *Solid State Sci.* **5**, 839 (2003), International Conference on Inorganic Materials 2002.
- [38] J. P. Perdew, K. Burke, and M. Ernzerhof, Generalized Gradient Approximation Made Simple, *Phys. Rev. Lett.* **77**, 3865 (1996).
- [39] D. R. Hamann, Optimized norm-conserving Vanderbilt pseudopotentials, *Phys. Rev. B* **88**, 085117 (2013).
- [40] M. van Setten, M. Giantomassi, E. Bousquet, M. Verstraete, D. Hamann, X. Gonze, and G.-M. Rignanese, The PseudoDojo: Training and grading a 85 element optimized norm-conserving pseudopotential table, *Comput. Phys. Commun.* **226**, 39 (2018).
- [41] N. Marzari and D. Vanderbilt, Maximally localized generalized wannier functions for composite energy bands, *Phys. Rev. B* **56**, 12847 (1997).
- [42] I. Souza, N. Marzari, and D. Vanderbilt, Maximally localized wannier functions for entangled energy bands, *Phys. Rev. B* **65**, 035109 (2001).
- [43] <https://sites.google.com/view/kazuma7k6r>.
- [44] E. Şaşıoğlu, C. Friedrich, and S. Blügel, Effective coulomb interaction in transition metals from constrained random-phase approximation, *Phys. Rev. B* **83**, 121101 (2011).
- [45] J. Yamauchi, M. Tsukada, S. Watanabe, and O. Sugino, First-principles study on energetics of c-BN(001) reconstructed surfaces, *Phys. Rev. B* **54**, 5586 (1996).
- [46] S. Baroni, S. de Gironcoli, A. Dal Corso, and P. Giannozzi, Phonons and related crystal properties from density-functional perturbation theory, *Rev. Mod. Phys.* **73**, 515 (2001).
- [47] A. D. Corso, Pseudopotentials periodic table: From H to Pu, *Comput. Mater. Sci.* **95**, 337 (2014).
- [48] G. Kresse and J. Furthmüller, Efficient iterative schemes for ab initio total-energy calculations using a plane-wave basis set, *Phys. Rev. B* **54**, 11169 (1996).
- [49] P. E. Blöchl, Projector augmented-wave method, *Phys. Rev. B* **50**, 17953 (1994).
- [50] G. Kresse and D. Joubert, From ultrasoft pseudopotentials to the projector augmented-wave method, *Phys. Rev. B* **59**, 1758 (1999).
- [51] T. Ozaki, Variationally optimized atomic orbitals for large-scale electronic structures, *Phys. Rev. B* **67**, 155108 (2003).
- [52] K. Momma and F. Izumi, VESTA3 for three-dimensional visualization of crystal, volumetric and morphology data, *J. Appl. Crystallogr.* **44**, 1272 (2011).
- [53] S. Matsuishi, Y. Toda, M. Miyakawa, K. Hayashi, T. Kamiya, M. Hirano, I. Tanaka, and H. Hosono, High-density electron anions in a nanoporous single crystal: $[\text{Ca}_{24}\text{Al}_{28}\text{O}_{64}]^{4+}(4e^-)$, *Science* **301**, 626 (2003).
- [54] M. Hirayama, S. Matsuishi, H. Hosono, and S. Murakami, Electrides as a New Platform of Topological Materials, *Phys. Rev. X* **8**, 031067 (2018).
- [55] K. P. Bohnen, R. Heid, and M. Krauss, Phonon dispersion and electron-phonon interaction for $\text{YBa}_2\text{Cu}_3\text{O}_7$ from first-principles calculations, *Europhys. Lett.* **64**, 104 (2003).
- [56] F. Giustino, M. L. Cohen, and S. G. Louie, Small phonon contribution to the photoemission kink in the copper oxide superconductors, *Nature (London)* **452**, 975 (2008).
- [57] P. B. Allen and R. C. Dynes, Transition temperature of strongly-coupled superconductors reanalyzed, *Phys. Rev. B* **12**, 905 (1975).
- [58] M. Imada and T. Miyake, Electronic structure calculation by first principles for strongly correlated electron systems, *J. Phys. Soc. Jpn.* **79**, 112001 (2010).
- [59] G. Kotliar, S. Y. Savrasov, K. Haule, V. S. Oudovenko, O. Parcollet, and C. A. Marianetti, Electronic structure calculations with dynamical mean-field theory, *Rev. Mod. Phys.* **78**, 865 (2006).
- [60] T. Tadano, Y. Nomura, and M. Imada, Ab initio derivation of an effective Hamiltonian for the $\text{La}_2\text{CuO}_4/\text{La}_{1.55}\text{Sr}_{0.45}\text{CuO}_4$

- heterostructure, *Phys. Rev. B* **99**, 155148 (2019).
- [61] M. Hirayama, Y. Yamaji, T. Misawa, and M. Imada, Ab initio effective Hamiltonians for cuprate superconductors, *Phys. Rev. B* **98**, 134501 (2018).
- [62] M. Hirayama, T. Misawa, T. Ohgoe, Y. Yamaji, and M. Imada, Effective Hamiltonian for cuprate superconductors derived from multiscale ab initio scheme with level renormalization, *Phys. Rev. B* **99**, 245155 (2019).
- [63] P. Werner, R. Sakuma, F. Nilsson, and F. Aryasetiawan, Dynamical screening in La_2CuO_4 , *Phys. Rev. B* **91**, 125142 (2015).
- [64] S. W. Jang, H. Sakakibara, H. Kino, T. Kotani, K. Kuroki, and M. J. Han, Direct theoretical evidence for weaker correlations in electron-doped and Hg-based hole-doped cuprates, *Sci. Rep.* **6**, 33397 (2016).
- [65] F. Nilsson, K. Karlsson, and F. Aryasetiawan, Dynamically screened Coulomb interaction in the parent compounds of hole-doped cuprates: Trends and exceptions, *Phys. Rev. B* **99**, 075135 (2019).
- [66] E. Pavarini, I. Dasgupta, T. Saha-Dasgupta, O. Jepsen, and O. K. Andersen, Band-Structure Trend in Hole-Doped Cuprates and Correlation with $T_{c\text{max}}$, *Phys. Rev. Lett.* **87**, 047003 (2001).
- [67] K. Nakamura, Y. Nohara, Y. Yoshimoto, and Y. Nomura, Ab initio *GW* plus cumulant calculation for isolated band systems: Application to organic conductor $(\text{TMTSF})_2\text{PF}_6$ and transition-metal oxide SrVO_3 , *Phys. Rev. B* **93**, 085124 (2016).
- [68] K. Nakamura, Y. Yoshimoto, T. Kosugi, R. Arita, and M. Imada, Ab initio derivation of low-energy model for κ -ET type organic conductors, *J. Phys. Soc. Jpn.* **78**, 083710 (2009).
- [69] K. Nakamura, R. Arita, and M. Imada, Ab initio derivation of low-energy model for iron-based superconductors LaFeAsO and LaFePO , *J. Phys. Soc. Jpn.* **77**, 093711 (2008).
- [70] Y. Nohara, S. Yamamoto, and T. Fujiwara, Electronic structure of perovskite-type transition metal oxides LaMO_3 ($M = \text{Ti} \sim \text{Cu}$) by $U + \text{GW}$ approximation, *Phys. Rev. B* **79**, 195110 (2009).
- [71] T. Fujiwara, S. Yamamoto, and Y. Ishii, Generalization of the iterative perturbation theory and metal-insulator transition in multi-orbital Hubbard bands, *J. Phys. Soc. Jpn.* **72**, 777 (2003).